A&A 545, A60 (2012)
DOI: 10.1051/0004-6361/201219356

Astronomy & Astrophysics

The 10 μm band in amorphous $MgSiO_3$: the influence of medium-range structure, defects and thermal processing

S. P. Thompson, J. E. Parker, and C. C. Tang

Diamond Light Source, Harwell Science and Innovation Campus, Chilton, Didcot, Oxfordshire OX11 0QX, UK
e-mail: stephen.thompson@diamond.ac.uk

Received 5 April 2012 / Accepted 12 July 2012

ABSTRACT

Context. Variations in the 10 μm amorphous silicate band profile between different environments have been variously attributed to differences in composition, grain processing or macroscopic constitution (e.g. compact versus aggregate grains). However the relationship with mineralogical structure has remained poorly defined.

Aims. The relationship between the 10 μm band and medium-range (~2–20 Å) structure is investigated.

Methods. Synchrotron X-ray scattering, Fourier transform infrared and Raman spectroscopy are used to relate changes in medium-range structure to changes in the 10 μm band profile for amorphous $MgSiO_3$ annealed at temperatures leading up to crystallisation.

Results. Raman and X-ray data show a build up of strain within the silicate network, which is released between ~400–550 °C, causing a relaxation of both the Si-O-Si bond angle and Si-O bond length. Decomposing the 10 μm band at each temperature step shows SiO_3 is the initially dominant component and increases in proportion as other species become incorporated into the silicate structure. However at ~400 °C the proportion of SiO_3 decreases as species with greater numbers of non-bridging oxygens form. The coincidence with strain release implies a breakup of larger tetrahedral structures.

Conclusions. We identify a correspondence between the spectral response at 10 μm of amorphous $MgSiO_3$ and the evolution of its structural state at medium-range distances. The dependence of the 10 μm band on medium-range structure may account for the hitherto poor correlation between composition and band behaviour, variations in the 10 μm band observed in other silicates of similar compositions, or, between observed bands in different astronomical settings.

Key words. X-rays: ISM – dust, extinction – circumstellar matter – comets: general

1. Introduction

1.1. The 10 μm silicate band

Amorphous silicate dust grains exhibit a characteristic mid-IR feature near 10 μm that is ubiquitous, strong and broad. It is seen in absorption against bright background sources (e.g. galactic centre, protostellar cores) and in emission, or self absorption, in the circumstellar regions of many O-rich, cool, red giant stars and supergiants, with a considerable spread in peak position and width being observed between objects. O-rich asymptotic giant branch (AGB) stars are the main source of interstellar medium (ISM) silicates (Draine 2003). Silicates in evolved stars appear to be well modelled by Mg-rich olivine $(Mg, Fe)_2SiO_4$ compositions (Demyk et al. 2001), while in young stars they appear better modelled by Mg-rich pyroxene $(Mg, Fe)SiO_3$ compositions (Demyk et al. 1999). For T Tauri and Herbig Ae/Be stars, variations in the shape and strength of the 10 μm feature are often interpreted as a measure of grain growth (Natta et al. 2007) since the feature should theoretically become wider and weaker with increasing grain size. Once injected in to the ISM, any crystalline silicates formed in circumstellar regions are thought to undergo amorphization by structurally disruptive processes such as ion implantation (Demyk et al. 2001, 2004; Brucato et al. 2003; Jäger et al. 2003; Bringa et al. 2007; Davoisine et al. 2008).

Diffuse ISM silicates are best represented by the 10 μm profile of the red supergiant μ Cephei (Roche & Aitken 1984), while in colder denser regions (e.g. molecular clouds) absorption profiles are better represented by the Orion Trapezium region profile (Forrest et al. 1975). The main differences being in peak position and feature width (Chiar & Tielens 2006), though dense clouds and young stellar objects both show additional absorption in the long wavelength side of the band attributed, respectively, to a separate population of non-volatile dust species and to ice. In protoplanetary disks variations in band morphology and peak position, along with fine-structure features due to evolving crystallinity (Dullemond et al. 2006; Sargent et al. 2006; Shupping et al. 2006; Watson et al. 2009; Riaz 2009) suggests amorphous grains undergo some form of processing (e.g. thermal annealing, Nuth & Johnson 2006) and may then be deposited into the surrounding molecular cloud and hence into the general ISM through protostellar winds (Tielens 2003).

Amorphous silicate 10 μm features are also observed in extragalactic environments, including Seyfert galaxies (e.g. Laurent et al. 2000; Clavel et al. 2000), quasars (Hao et al. 2005), luminous and ultraluminous IR galaxies (Genzel et al. 1998; Rigopoulou et al. 1999; Tran et al. 2001) and certain mid-IR detected, optically invisible, high luminosity galaxies (Houck et al. 2005). The broad silicate features observed in many type 1 and 2 active galactic nuclei (AGN) are thought to be associated with the obscuring torus surrounding the accreting massive black hole (Veilleux 2004). While AGB stars dominate dust production in the local universe, large amounts of dust from AGB stars cannot be accumulated within ~1 Gyr of the birth of the first generation of low-mass stars (Morgan & Edmunds 2003). However, quasar host galaxies ($z \sim 6$) show evidence for 10^8–10^9 $M_\odot$ of dust being heated by star formation (Priddey et al. 2003; Beelen et al. 2006), probably produced by a combination of quasars (Elvis et al. 2002) and supernovae (Sugerman et al. 2006). The

10 μm profiles observed for AGN silicates (e.g. Strum et al. 2005) often differ significantly from the ISM profile, with varying peak wavelengths between 10 and 11.5 μm attributed to additional dust components (Markwick-Kemper et al. 2007), or large porous grains (Smith et al. 2010) due to grain growth by coagulation (Maiolino et al. 2001).

In modelling the 10 μm band (e.g. Bouwman et al. 2001; van Boekel et al. 2005) the light absorption for several populations of compact and/or hollow amorphous and crystalline silicate spheres of small and large sizes is calculated and used to fit observed profiles. If adequate fits cannot be obtained using just silicates, other likely grain species or materials are then often invoked. Alternatively, the shape, position and strength of the 10 μm band can also be modelled using small-mass composite fractal-like aggregates (e.g. Voshchinnikov & Henning 2008) where fits are obtained by varying aggregate properties such as porosity, size and composition. However, while observed profiles differ between environments, the silicates used in these procedures are generally assumed to be mineralogically similar, occupying some form of implied "standard" amorphous state represented by the optical properties derived from laboratory measurements (e.g. Henning et al. 1999), or by "astronomical silicate" derived from the Trapezium profile (Draine & Lee 1984; Weingartner & Draine 2001). The pool of laboratory data on which observational analyses are based is however finite; and it has long been recognised that laboratory analogues manufactured by different methods show subtle differences in their measured spectra. This point gained prominence with the discovery of crystalline circumstellar silicates, since the strength, position and width of the narrow absorption features associated with crystalline structure exhibit an obvious dependency on their method of preparation and composition, with structural defects likely to play an important role (Imai et al. 2009). Less progress however has been made in quantitatively determining the extent of such effects on the spectral behaviour of amorphous silicates. Consequently, differences in amorphous structure may play a hitherto poorly defined role in determining the observational properties of the 10 μm band for non-crystalline silicate grains. Despite many experimental studies, only minor dependencies of optical properties with chemical composition have thus far been established for amorphous silicates (e.g. Dorschner et al. 1995; Coupeaud et al. 2011). Furthermore, annealing experiments on fixed compositions (e.g. Brucato et al. 1999, 2002; Thompson et al. 2002, 2007) show obvious changes to the 10 μm band profile, width and peak position, indicating changes to internal properties are also driven by external environmental conditions. In this paper we present laboratory results that relate the behaviour of the 10 μm band of a sample of amorphous $MgSiO_3$, annealed at different temperatures, with changes occurring in its medium-range structure.

1.2. Si-O stretch modes and silicate structure

Silicate resonances near 10 μm are due to Si-O stretching vibrations within tetrahedral structures. Their frequencies are however modified depending on whether the O atoms are shared with neighbouring tetrahedra and should in principle provide direct information on the distribution of tetrahedral connectivity (Nuth & Hecht 1990; Jäger et al. 1994; Thompson 1996). In crystalline silicates the distribution of the number of bridging and non-bridging oxygen atoms per tetrahedron (BO/T and NBO/T respectively, with BO/T+NBO/T = 4) is strongly peaked around a single value determined by the bulk composition, while in amorphous silicates a wider distribution is usual (Gurman 1990).

Table 1. Silicate Si-O vibrational wavelengths.

λ (μm)	Species	NBO/T	Central λ (μm)	Structural elements
11.49–11.9	SiO_4	4	11.69	single tetrahedra
10.87–11.23	Si_2O_7	3	11.05	double tetrahedra
10.0–10.52	SiO_3	2	10.26	single-linked chains
9.09–9.52	Si_2O_5	1	9.31	sheets
8.33–9.38	SiO_2	0	8.86	3-D network

Notes. Species refers to the tetrahedral component of the silicate and NBO/T is its number of non-bridging oxygen atoms per tetrahedral unit. Data drawn from Brawer & White (1975), Virgo et al. (1980), Kusabiraki & Shiraishi (1981), Kusabiraki (1987), Jäger et al. (1998), Aguiar et al. (2009).

Table 1 lists typical ranges for the peak positions of the Si-O stretch vibrations for each NBO/T derived from various silicates. Although each species exhibits a range of wavelengths over different materials, the average central wavelength is almost linear with increasing NBO/T. In effecting changes to the relative distribution of BO/T and NBO/T, differences in internal structure ought to have a measurable effect on observable characteristics such as peak position and band morphology.

1.3. Medium-range structure

Amorphous materials are characterised by the absence of long-range order. However, the forces linking atoms are the same in both crystalline and non-crystalline solids and so non-crystalline materials are only disordered in respect of some aspect of their structure; which in practice comes down to determining what degree of order can be identified experimentally at different length scales. Removing the requirement for long-range order however does not necessarily result in total disorder. A certain limited order – termed short-range order – often remains, defined by nearest neighbour interatomic correlations, typically ranging over ~1–2 Å. Short-range order is represented by a basic structural building block which, in silicates, is the Si-O tetrahedron and at this level silicates are highly ordered. However, many non-crystalline solids also exhibit a degree of structural correlation over distances typically from ~2 Å out to 10 or 20 Å due to larger structural features such as rings or chains (Philips 1979; Lucovski & Galeener 1980; Wright 1990). However the parameters governing the way these link together are highly variable (Mozzi & Warren 1969) and it is with this medium-range interconnection of tetrahedra that disorder can begin.

There are two competing models for structural arrangement beyond the first short-range coordination distance in silicates. In the Zachariasen-Warren model (Zachariasen 1932; Warren 1933, 1934; Warren et al. 1936) tetrahedra are linked together in a statistically disordered way to form a continuous random network with no long-range periodicity, but which can nevertheless exhibit ring and chain structures. Alternatively, Lebiediev (1921), Randall et al. (1930a,b) and Valenkow & Porai-Koshitz (1936) proposed a model involving ultrafine microcrystals (~15–20 Å), embedded within a continuous random network which links between the microcrystal surfaces in a statistically random way. In this model amorphous silicates are domain structured materials (Verweij & Konijnendijk 1976) with medium-range structure emerging naturally with the presence of, or formation and

growth of, dispersed microcrystals. The two models however only really differ in the size and number of the microcrystalline regions and real silicates are likely to embody regions that correspond to a greater or lesser degree to one or the other extreme (Gaskell 1986).

Previously (Thompson 2008), the presence and extent of medium-range structure in three amorphous Mg-silicates annealed over coarse temperature intervals was investigated using X-ray absorption near edge structure (XANES) spectroscopy and by X-ray scattering. The XANES data showed the growth of medium-range structure from 5 to 10 Å; while certain X-ray scattering features at low values of the X-ray scattering vector were identified with correlations between medium-range structures with differing tetrahedral connectivity. In the present work, new low X-ray wavevector measurements are combined with IR and Raman spectroscopy to investigate the relationship between medium-range structure and spectroscopic behaviour at 10 μm for a sample of fixed amorphous $MgSiO_3$ composition, with structural change being driven by thermal annealing over finer temperature intervals.

2. Experimental details

2.1. Sample manufacture

For this experiment amorphous $MgSiO_3$ was produced from a sol-gel obtained by mixing 0.1 molar solutions of $MgCl_2$ and Na_2SiO_3, according to a procedure that has been well documented previously (Thompson et al. 2002, 2003, 2007). After washing and drying the gels in air at 75 °C for 24 h, the precipitate yields large irregular glassy solids which were then ground to form a fine-grained powder of which separate batches were annealed at discrete temperatures between 100 °C and 700 °C using a Carbolite tube furnace. The annealing time at peak temperature for each sample was ~17.5 ± 1 h. This method of sample preparation while obviously not mimicking the formation conditions of cosmic grains, has been found by us to consistently produce an amorphous silicate with reproducible properties providing good parity between different investigations. As such, the sample prepared for the present work is equivelent to the Product I silicate refered to in Thompson (2008), Thompson et al. (2007) and the $MgSiO_3$ silicates in earlier works (Thompson et al. 2002, 2003; Thompson & Tang 2001).

2.2. Vibrational spectroscopy

Raman spectra were measured on a Horiba Jobin Yvon confocal LabRam 800 employing a 632.817 nm laser, 600 line grating and 50× objective lens. For ease of comparison, the datasets were scaled to the height of the dominant feature at ~670 cm^{-1} and the trough minimum at 530 cm^{-1}. In the literature, Raman spectra are usually discussed in terms of wavenumber (cm^{-1}), while for IR spectra wavelength (μm) is more common. For ease of comparison with both published works and the IR data presented later, the initial discussion of the Raman data in Sect. 3.1 will be in terms of wavenumber with wavelength equivalents given in parenthesis. Mid-IR spectra were collected using a Bruker Vertex 70 FT-IR equipped with a Harrick diamond crystal attenuated total reflectance (ATR) accessory. ATR spectra were converted to transmission absorption equivalents using Bruker's OPUS software[1]. Although ATR is well suited to fine particulate samples, as they make good contact with the ATR crystal, the quantity of material in contact with the crystal cannot be tightly controlled. Thus in order to make comparisons between the annealed samples, the peak intensity in the 10 μm band for each sample was normalised to the background intensity at 8 μm and scaled to the band maximum.

[1] http://www.brukeroptics.com/opus.html

2.3. Synchrotron X-ray scattering

For X-rays of wavelength λ, away from an absorption edge, many non-crystalline materials exhibit a scattering peak at low values of the X-ray scattering wavevector, $\boldsymbol{k}$ ($k = |\boldsymbol{k}| = 4\pi \sin\theta\lambda^{-1}$), characteristic of medium-range ordering (Elliot 1991). The range in k where these features occur can be approximated using the Debye expression for X-ray scattering by a completely random arrangement of atoms,

$$I(k) = \Sigma_n^N \Sigma_m^N f_n f_m \frac{\sin kr_{nm}}{kr_{nm}} \quad (1)$$

where f_n and f_m are the atomic scattering contributions from atoms n and m and r_{nm} their separation distance. The $\sin kr/kr$ term has its first $kr > 0$ maximum at $kr \simeq 7.725$ and thus the limiting magnitude of the scattering vector for sampling medium-range structure will be $k_c = 7.725/r$. In silicates the Si-O bond length, r_{Si-O}, is typically ~1.6 Å and we can define a typical single medium-range order generating element, for example, to be a cluster of three tetrahedra sharing a common O atom at one vertex and represent this by a sphere centred on one Si atom, whose surface touches the centres of the other two tetrahedra. Thus, $r \simeq 2r_{Si-O}$ and features in the scattering pattern for $k \leq k_c \sim 2.5$ $Å^{-1}$ can be attributed to medium-range inter-tetrahedral structure.

Low-k X-ray scattering measurements were performed on Beamline I11 (Thompson et al. 2009) at the Diamond Light Source synchrotron. This receives low divergence, high intensity X-rays from a 22-pole undulator source located within a straight section of the 3 GeV storage ring and employs a concentric 3-circle diffractometer with 45 analysing crystal-detector pairs, arranged in groups of nine, spread over five arms distributed around the 2θ-circle. This provides an "intensity recovery" measurement geometry to speed up collection times and also removes unwanted background scattering contributions. The low-noise, wide dynamic range detectors (Tartoni et al. 2008) used in conjunction with the analyser crystals means that nearly all of the measured scattering intensity away from the primary beam direction (i.e. above ~1 $Å^{-1}$ in Fig. 3) originates from the sample, while the high intensity undulator source allows scattering data to be collected with a much higher statistical quality than was available in the earlier Thompson (2008) study. Furthermore the low background, low noise signal means that the I11 instrument is much more sensitive to the presence of weakly scattering, trace level or crystallising phases (Thompson et al. 2009). Samples were loaded onto a Si wafer cut along the forbidden 520 crystallographic direction to suppress diffraction from the wafer itself. This was mounted at the centre of the instrument and inclined at a fixed angle of 3° to the incident beam. To increase sampling statistics the sample was spun about the axis normal to the substrate surface. Scattering data were then collected using $E = 20$ keV monochromatic X-rays and constant velocity scanning of the 2θ circle (20 min per sample) with data collected at 0.001° intervals. Since the amorphous scattering features are broad, the datasets were rebinned to 0.01° intervals to further improve counting statistics without worsening feature resolution. The angle-dispersed data were then converted

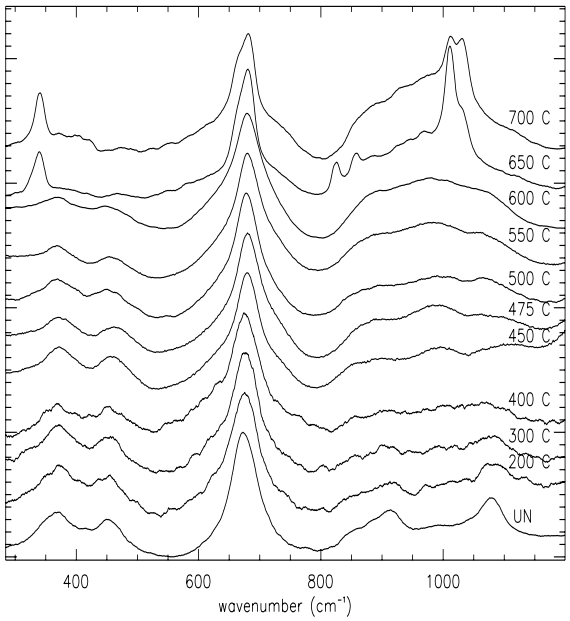

Fig. 1. Raman spectra for samples of $MgSiO_3$ annealed at increasing temperatures for 17.5 ± 1 h each. Spectra are scaled to height of the strong feature at ~670 cm^{-1} and trough minimum at ~530 cm^{-1} and offset in y-axis direction for clarity.

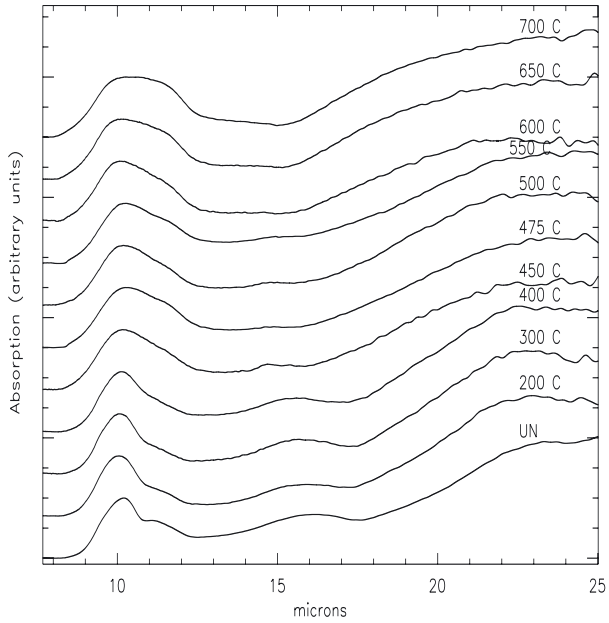

Fig. 2. IR spectra measured for $MgSiO_3$ for increasing annealing temperatures. For clarity, each spectrum is scaled to the band maximum at 10 μm and background at 8 μm and offset in y-axis direction.

to energy-independent X-ray scattering wavevector space via the relation $k = 4\pi \sin\theta\lambda^{-1}$, where θ is half the measured 2θ angle and $\lambda(\text{Å}) = 12.394E^{-1}$; with the units of k given in Å^{-1}.

3. Results

3.1. Vibrational spectroscopy

Figure 1 shows the Raman spectra for each annealed sample, from which three distinct regions can be identified:

1. *800–1100 cm^{-1} (12.5–9.09 μm).* This region sub-divides into a 800–1000 cm^{-1} (12.5–10.0 μm) band due to Si-O_{NBO} stretching vibrations and a 1000–1100 cm^{-1} (10.0–9.09 μm) band due to asymmetric Si-O_{BO} stretch modes (Furukawa et al. 1981). In the unprocessed sample two strong broad features are present at ~900 and ~1100 cm^{-1} (11.11 and 9.09 μm), which decrease in intensity at 300 °C and are replaced by a broad feature spanning the entire region up to 600 °C, thereafter more structured features emerge. The change from two Raman features at ~900 and ~1100 cm^{-1} to a broad feature spanning the entire 800 to 1100 cm^{-1} region indicates that the BO/T and NBO/T distribution changes with annealing. Unfortunately the Raman signal in this region for samples annealed between 200 and 500 °C is too weak due to strong sample photoluminescence to allow the spectra to be decomposed into separate components attributable to different NBO/T species.
2. *500–800 cm^{-1} (20–12.5 μm).* Features in this region are due to bridging Si-O-Si vibrations and are therefore directly related to medium-range structure. The silicate spectra in this region are all dominated by a single strong feature near ~670 cm^{-1} (14.92 μm). In crystalline pyroxenes with orthorhombic *Pbca* and monoclinic $P2_1/c$ symmetries two crystallographically distinct chain structures exist and differences in the Si-O-Si intertetrahedral angle, ϕ_{T-T}, and the r_{Si-O} bondlength result in a splitting of the 670 cm^{-1} feature. However the low frequency component is usually weakest and in Fig. 1, a weak shoulder can be discerned at ~650 cm^{-1} for the 700 °C sample. Other related features also form above 600 °C, notably the doublet near 850 cm^{-1} which coincides with the internal Si-O_{NBO} stretch in the isolated tetrahedra of forsterite (Kalampounais et al. 2008), while the doublet at ~1050 cm^{-1} arises from crystallographically distinct chain structures in *Pbca* pyroxene (Wang et al. 2001). The absence of these crystalline features below 650 °C confirms the absence of long-range structural correlations in the lower temperature samples.
3. *<500 cm^{-1} (>20 μm).* Between 100–400 cm^{-1} (100–25 μm) features originate from lattice mode vibrations produced by translation of the Mg cation relative to the tetrahedral network (Wang et al. 2001). Below 650 °C this low frequency region in Fig. 1 is dominated by two features at ~370 and ~450 cm^{-1} (27.03 and 22.22 μm) which, with increasing annealing temperature, shift slightly towards lower frequencies and diminish in strength, being replaced by a single strong feature at ~339 cm^{-1} (29.5 μm) above 650 °C indicative of a change in the environment surrounding the Mg atoms.

Figure 2 shows the IR spectra at each annealing temperature. The overall 10 μm band profile becomes increasingly broader on its long wavelength side with each temperature increase, while a broad feature at ~16 μm simultaneously shifts to shorter wavelength, becoming progressively weaker up to ~500 °C. Above this temperature a very broad increase in the scattering beyond ~16 μm occurs. No fine structure features associated with crystallisation form in the 10 μm region.

3.2. Low-k X-ray scattering

Figure 3 shows the low-k X-ray scattering data for each sample. Weak Bragg diffraction peaks, located on the broad amorphous scattering, due to developing crystallinity are evident at 600 °C. Using a search-match client to the International Centre for Diffraction Data (ICDD) PDF4$^+$ database, all the

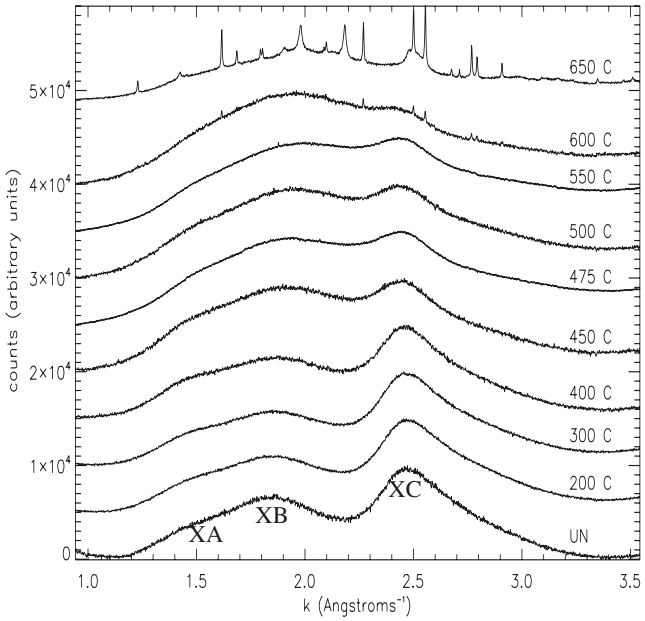

Fig. 3. Evolution of low-k X-ray scattering from $MgSiO_3$ as a function of annealing temperature. Three features at ~1.4, ~1.8 and ~2.5 Å^{-1} labelled XA, XB and XC are present below the limiting scattering vector magnitude of ~2.5 Å^{-1} for sampling medium-range structure. Patterns for each sample are offset in y-axis direction for clarity.

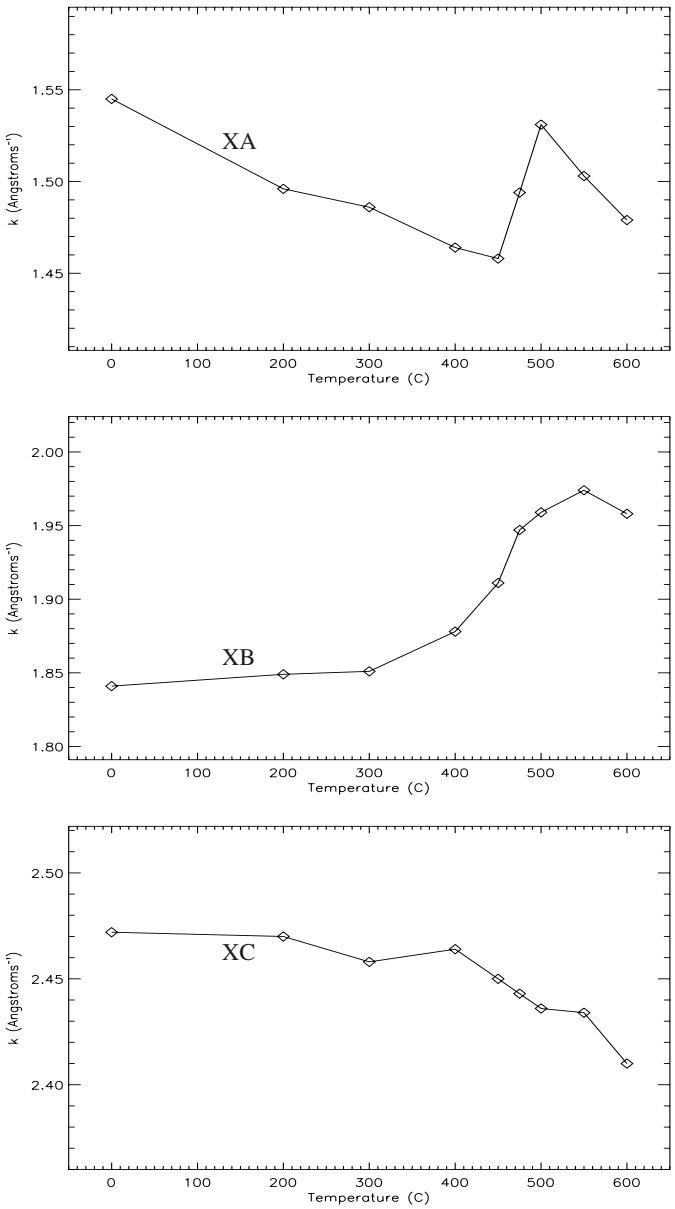

Fig. 4. Evolution in peak position of the $MgSiO_3$ low-k X-ray scattering features in Fig. 3 as a function of annealing temperature.

Bragg peaks at this annealing temperature were accounted for by forsterite (Mg_2SiO_4), while at 650 °C, a number of additional peaks due to enstatite ($MgSiO_3$) were also identified. The temperature at which crystalline diffraction is observed in the X-ray data appears slightly lower than that reported in the previous (Thompson 2008) study. However this is likely due to a combination of differences in the furnace aperatus used to anneal the samples and the increased sensitivity of the Diamond I11 instrument over the Daresbury Laboratory (SRS Station 2.3) one used previously. Below 600 °C only broad features are recorded: a weak shoulder at ~1.4 Å^{-1} and two strong features at ~1.8 and ~2.5 Å^{-1} (labelled XA, XB and XC), all of which are located at or below the limiting magnitude of the X-ray scattering vector for medium-range structure. Their positions as a function of annealing temperature are plotted in Fig. 4 and clearly show medium-range scale changes occurring for temperatures at or above ~400 °C.

4. Discussion

4.1. Structural evolution

4.1.1. The 670 cm^{-1} Raman band: intertetrahedral strain

Disorder in silicates arises mostly from variations in the Si-O-Si bond angle and torsion angle distributions between adjacent tetrahedra. Due to its association with medium-range structure, shifts in the position of the 670 cm^{-1} band can be attributed to changes in the intertetrahedral arrangement. Specifically, the peak frequency shifts to higher values as the intertetrahedral bond angle, ϕ_{T-T}, steepens (Serghiou et al. 2000a,b, 2004, and references therein) and Fig. 5 plots the peak position of this band as a function of annealing temperature. Clearly visible is a general trend towards higher frequency, however also apparent are anomalously large frequency shifts between 400 and 500 °C. In low-pressure crystalline silicates ϕ_{T-T} usually varies from 134° to 150° (with some extremes near 160°), with various studies indicating a simultaneous narrowing of ϕ_{T-T} (and decrease in r_{Si-Si}) as r_{Si-O} increases (McDonald & Cruickshank 1967; Pant 1968; Pant & Cruickshank 1968; Gibbs et al. 1972; Boisen et al. 1990). For example, in α-quartz and α-cristobalite ϕ_{T-T} is around 144°, with an average r_{Si-O} of 1.61 Å, while in α- and β-$Na_2Si_2O_5$, these reduce to 135–139° and ~1.64 Å respectively and in crystalline Na_2SiO_3, to 134° and ~1.67 Å. Further decreases in ϕ_{T-T} and increases in r_{Si-O} are similarly observed as Na content increases (Yuan & Cormack 2003). Such changes in ϕ_{T-T} and r_{Si-O} arise from the interplay between the attractive Si-O atomic orbit bonding, bonded Si-O coulombic repulsion and non-bonded Si-Si repulsion (Yuan & Cormack 2003). In amorphous SiO_2, the ϕ_{T-T} distribution is broad due to the presence of high internal strain, while the addition of a network modifier such as Na^{2+} releases the strain and allows ϕ_{T-T} to approach equilibrium values. Thus we interpret the general shift to higher frequency with temperature in Fig. 5 as a progressive narrowing

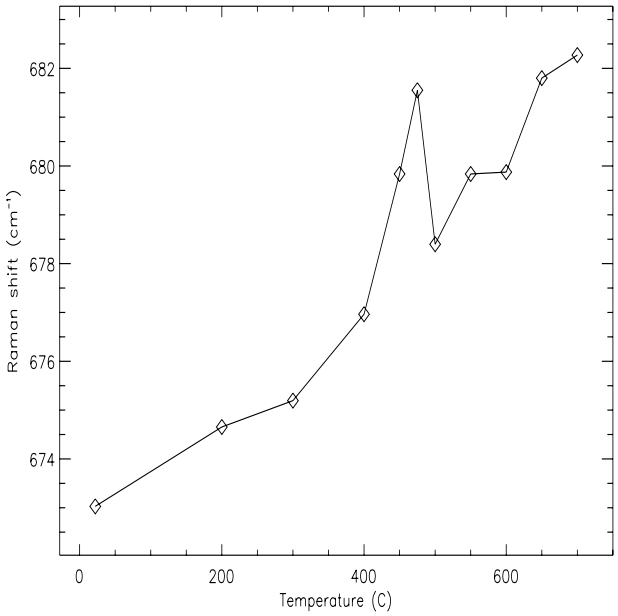

Fig. 5. Shift in peak position of $MgSiO_3$ 670 cm^{-1} medium-range order Raman feature as a function of annealing temperature. Shifts towards higher frequencies are characteristic of a narrowing of the Si-O-Si bond angle and a shortening of the Si-O bond distance. The sharp decrease between 475 and 500 °C is attributed to strain release.

of ϕ_{T-T} and lengthening of r_{Si-O}, both of which should increase the strain within the silicate structure. The sudden decrease in frequency between 475 and 500 °C can then be understood as strain release, which as we show below, arises from structural re-ordering.

4.1.2. Low-*k* scattering: medium-range structure

To interpret the X-ray features, two characteristic lengths, r and D, can be directly obtained:

$$kr \simeq 2.5 \quad (2)$$

and

$$D = 2\pi/k. \quad (3)$$

Equation (2) is an empirical relation derived from various amorphous systems that relates the position of the first scattering feature with the short-order bondlength (Wright et al. 1985, 1991; Elliot 1992; Ossi 2003) and for the first of the low-k features (XA) was found previously (Thompson 2008) to correspond well to r_{Si-O}, while D is simply the Bragg diffraction equation expressed in k-space. In the pseudo-Bragg interpretation of low-k scattering (Ossi 2003) the relative arrangement, over large distances, of regions that are themselves ordered over the medium-range results in a quasi-regular variation of electron density over some distance D that is analogous to the regular lattice plane spacings of crystalline phases. This gives rise to feature positions in amorphous materials which often lie almost coincident with the most intense diffraction peak of their corresponding crystal phase and can be used to associate D with structural components. Values of r_{XA} and D for XB and XC are shown in Fig. 6.

As was predicted by the strain interpretation of the shift in the 670 cm^{-1} Raman band, the shift in XA using Eq. (2) reveals a progressive stretching of r_{Si-O} from ~1.62 Å to ~1.71 Å as annealing temperatures increase up to 450 °C. However, between this temperature and 500 °C there is a shortening of r_{Si-O},

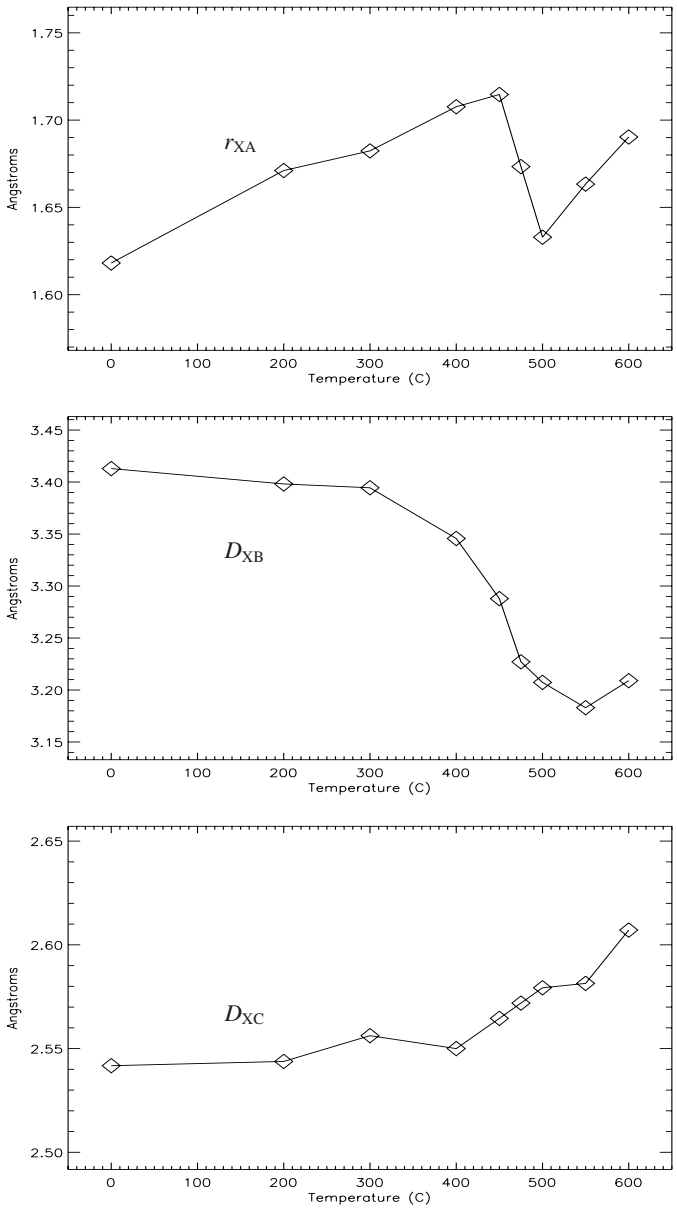

Fig. 6. Evolution of real-space lengths derived from low-k X-ray scattering: Si-O bond length r_{XA} and pseudo-Bragg distances D_{XB} and D_{XC} as a function of annealing temperature for $MgSiO_3$.

consistent with strain release from the network in the region of 400–500 °C. Above 500 °C r_{Si-O} lengthens again. The length D_{XA} (not plotted) ranges from 4.07 Å in the unprocessed sample to 4.23 Å in the 600 °C sample and follows the same behaviour as r_{XA}. By comparison with the crystal phase d-spacings of the strongest crystalline Bragg peaks for quartz, forsterite and various enstatites given in Table 2, D_{XA} could be attributed to scattering from cristobalite-like structures, however in cristobalite r_{Si-O} never exceeds ~1.61 Å (Peacor 1973; Kuniaki 1990). Alternatively, D_{XA} is close to the second Si-O distance in enstatite (i.e. from the Si atom in one tetrahedron to the second O atom in a linked neighbour; and where r_{Si-O} also ranges from ~1.51 to ~1.82). D_{XA} could therefore also be interpreted as scattering from pseudo-Bragg planes defined by the SiO_3 arrangement. The change in r_{XA} thus appears more likely associated with tensions within the constituent SiO_3 chain structures causing the Si-O tetrahedra to distort.

Table 2. *d*-spaces of strongest diffraction peaks for representative Mg-silicate minerals.

Mineral	*d* (Å)	*hkl*-index
Cristobalite	4.0474	101
Quartz	3.3436	101
Forsterite	2.4557	112
Monoclinic		
Enstatite	2.9808	22-1
Orthorhombic		
Enstatite 1	2.4338	112
Enstatite 2	3.1486	221
Enstatite 3	3.0745	121
Antigorite	3.6522	004
Lizardite	2.5001	111

Notes. Cristobalite and quartz (SiO_2): network formers; forsterite (Mg_2SiO_4): isolated tetrahedra; enstatite ($MgSiO_3$): chain forming; serpentine minerals antigorite and lizardite ($Mg_3Si_2O_5(OH)_4$): sheet forming.

The length D_{XB} starts with a value close to the *d*-space of quartz and decreases with temperature towards a value closer to orthorhombic enstatite. This could reflect a depolymerisation from NBO/T = 0 to NBO/T = 2, but given the absence of any significant amount of SiO_2 from the 10 μm band decompositions (see next section) and the similarity in behaviour of XB to XA, it is more probable that D_{XB} also relates entirely to NBO/T = 2 SiO_3 structures. Indeed, assuming the amorphous arrangement to be isotropic, the average volume per scattering unit should scale in proportion to k^{-3} (i.e. according to D^3; Louzguine et al. 2005) and the decrease in D_{XB} towards a minimum at ~500 °C, likely reflects the overall evolution of SiO_3 regions towards their equilibrium crystalline packing distances.

Finally, feature XC does not show the same evolution as XA or XB, though it does show a change in behaviour near ~400 °C. By the same argument as above, the behaviour of D_{XC} implies a marked increase in average volume surrounding the scattering unit from ~400 °C onwards. Given that both XA and XB appear to originate from SiO_3 structures, the different behaviour of D_{XC} may reflect structural changes involving other tetrahedral species and shows a range of values consistent with forsterite. However D_{XC} is also consistent with other silicate mineral structures (e.g. enstatite and lizardite) and a more definitive association is difficult. We should also note that XC lies close to the theoretical medium-range limiting magnitude, k_c, of the X-ray scattering vector and therefore may possibly not be a true medium-range feature.

4.1.3. The 10 μm band

Figure 7 shows the wavelength position of maximum intensity of the 10 μm band in the measured IR spectra as a function of annealing temperature, obtained by reading off the position of the zero-crossing point of the first derivative of the raw data. Although initial annealing at 200–300 °C causes the maximum to shift to shorter wavelengths, there is a clear rise and maximal shift towards longer wavelength for the samples annealed from 300 to 550 °C. Furthermore, the broadening of the measured profiles at each temperature in Fig. 2 largely occurs on the long wavelength side, with little change in the position of the short-ward rise, which by reference to Table 1 points to the evolving profile being increasingly influenced by changes in the relative NBO/T distribution; all of which are suggestive of a possible relationship between the 10 μm band and the changes at the medium-range scale we have observed thus far in both the Raman and X-ray data.

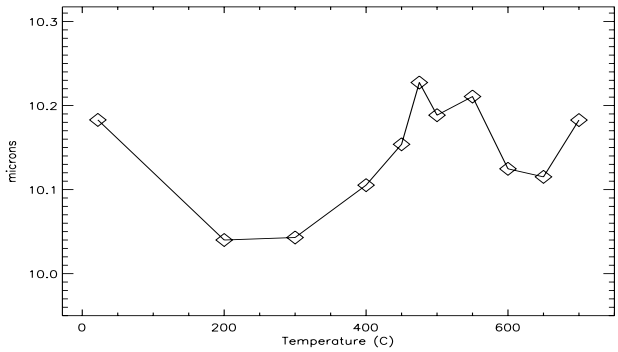

Fig. 7. Position of the maximum peak intensity of the 10 μm band for amorphous $MgSiO_3$ as a function of annealing temperature.

To quantify the changes in tetrahedral connectivity at each temperature step, a linear background was subtracted between 8.5 and 13 μm and the 10 μm band profile decomposed using five pseudo-Voigt functions (Stancik & Brauns 2008) with initial positions set to the central wavelength for each Si-O species listed in Table 1. Representative fits are shown in Fig. 8, while the wavelength positions for each component at each annealing temperature are plotted in Fig. 9 (wavelengths and fractional areas listed in Table 3). With the exception of SiO_2 which represents a minor constituent (see next paragraph), there appear to be systematic changes in wavelength around the 400 to 500 °C range, but which still fall within the ranges listed in Table 1 for each species.

Changes in the relative proportion, *n*, of each of the tetrahedral species as a function of annealing can be estimated from the area, *A*, of the band components since $n = \sigma A$, where σ is the IR cross section of the corresponding Si-O stretch (Mysen et al. 1982). These are plotted in Fig. 10 in terms of their fractional proportion of the total area of the band. Initially, the silicate is clearly dominated by SiO_3 tetrahedral arrangements, as would be expected by the sample stoichiometry. However, as expected for an amorphous silicate, other tetrahedral species are also present in significant amounts, in particular Si_2O_5 sheet and Si_2O_7 dimer units, while the fully connected SiO_2 and isolated SiO_4 end members represent only minor constituents. Annealing up to 300–400 °C further reduces the SiO_4, as well as Si_2O_7, as these presumably become incorporated into SiO_3 chain and Si_2O_5 sheet structures which both show increases in their relative content. However above this temperature the proportion of SiO_4 exhibits a sharp increase (and less so Si_2O_7) as the abundance of SiO_3 declines steeply, also accompanied by a reduction in Si_2O_5. The steep reduction in SiO_3 coincides with the abrupt changes seen in the 670 cm^{-1} Raman feature and the low-*k* derived r_{Si-O} bondlength, suggesting that it is the incorporation of tetrahedral units into SiO_3 chains at lower temperatures that strains the existing structures. For annealing temperatures above ~650 °C the SiO_4 content again increases sharply as both SiO_3 and Si_2O_5 show further reductions.

The rise in SiO_4 above 400 °C is consistent with both the earlier finding (Thompson & Tang 2001; see also Roskosz et al. 2009) that forsterite is the first crystalline phase to form from amorphous $MgSiO_3$ and with the search match identification of the Bragg peaks above ~600 °C in Fig. 3. Further confirmation of this can be seen in changes in the Mg K-edge XANES reported previously (Thompson 2008) and redrawn in Fig. 11,

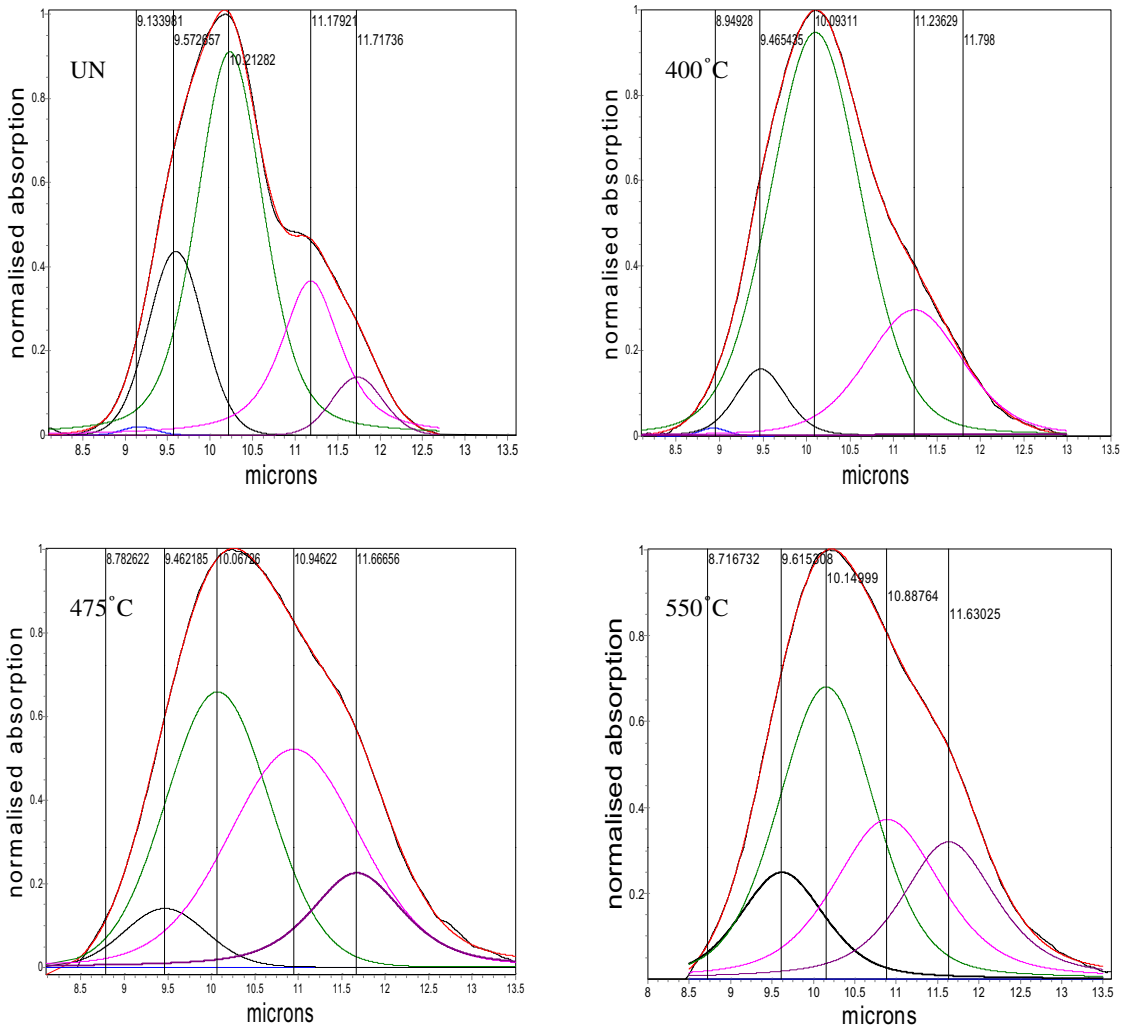

Fig. 8. Selected component decompositions of the 10 μm band for the as prepared $MgSiO_3$ (UN) and samples annealed at 400, 475 and 550 °C.

Table 3. IR Component feature positions and fractional areas for each tetrahedral species obtained from fits to the 10 μm band.

T(°C)	SiO_2		Si_2O_5		SiO_3		Si_2O_7		SiO_4	
	peak (μm)	area	peak (μm)	area	peak (μm)	area	peak (μm)	area	peak (μm)	area
700	8.663 ± 0.015	0.009	9.635 ± 0.01	0.139	10.230 ± 0.02	0.257	10.920 ± 0.013	0.254	11.695 ± 0.01	0.299
650	8.743 ± 0.04	0.012	9.631 ± 0.03	0.174	11.148 ± 0.04	0.389	10.946 ± 0.04	0.246	11.654 ± 0.01	0.179
600	8.853 ± 0.2	0.025	9.748 ± 0.02	0.147	10.099 ± 0.04	0.409	10.923 ± 0.04	0.246	11.649 ± 0.008	0.171
550	8.717 ± 0.006	0.002	9.615 ± 0.07	0.135	10.149 ± 0.02	0.395	10.888 ± 0.04	0.261	11.630 ± 0.02	0.207
500	8.799 ± 0.003	0.0003	9.711 ± 0.1	0.147	10.158 ± 0.03	0.463	10.925 ± 0.03	0.229	11.630 ± 0.02	0.159
475	8.783 ± 0.02	0.003	9.462 ± 0.07	0.041	10.067 ± 0.02	0.492	10.946 ± 0.04	0.286	11.667 ± 0.02	0.178
450	8.771 ± 0.02	0.002	9.532 ± 0.03	0.059	10.071 ± 0.02	0.557	11.002 ± 0.05	0.265	11.657 ± 0.02	0.116
400	8.949 ± 0.009	0.002	9.465 ± 0.003	0.071	10.093 ± 0.003	0.676	11.236 ± 0.006	0.242	11.798 ± 0.006	0.008
300	8.739 ± 0.05	0.003	9.514 ± 0.005	0.179	10.143 ± 0.004	0.626	11.204 ± 0.006	0.177	11.693 ± 0.02	0.014
200	9.007 ± 0.007	0.009	9.559 ± 0.006	0.195	10.168 ± 0.007	0.594	11.226 ± 0.005	0.166	11.667 ± 0.007	0.036
UN	9.134 ± 0.04	0.005	9.573 ± 0.006	0.165	10.213 ± 0.007	0.546	11.179 ± 0.004	0.232	11.717 ± 0.01	0.052

Notes. The area for each component is expressed as a fraction of the total band area.

which compares the local environments surrounding Mg atoms in two samples (an as prepared one and one annealed at 627 °C) with the Mg sites measured for crystalline enstatite ($MgSiO_3$) and forsterite (Mg_2SiO_4). Clear similarities exist between the Mg sites in enstatite and in the as prepared sample, while the Mg sites in the annealed sample are clearly those of crystalline forsterite. Taken together, these independent findings point to a process of phase separation that starts prior to crystallistaion, such that the evolving amorphous silicate would appear to be better represented by a domain structured model along the lines of that developed by Lebiediev, Randall and others as described in Sect. 1.3.

4.1.4. Role of hydration defects

The pre-cursor gel used to manufacture the silicate for these annealing experiments is formed in a watery environment using

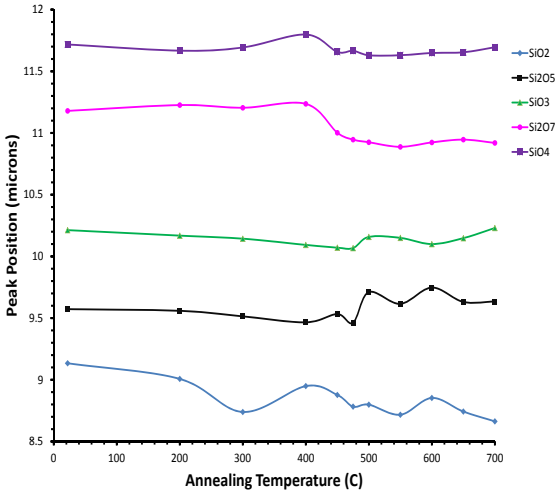

Fig. 9. Evolution of fitted peak positions for the $MgSiO_3$ 10 μm band decomposition in terms of Si-O tetrahedral component bands at each annealing temperature.

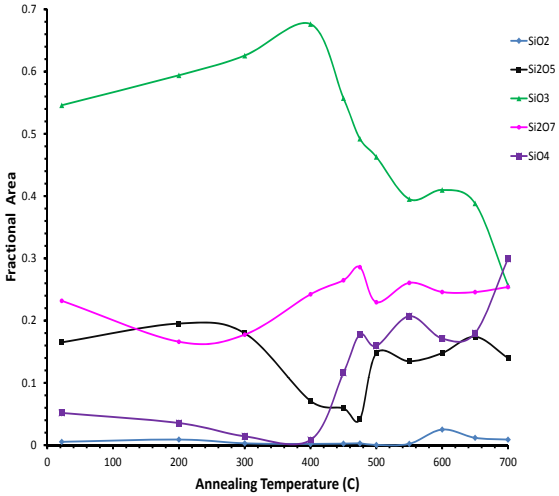

Fig. 10. Relative fractional areas of the IR band components for different Si-O tetrahedral species as a function of annealing temperature.

reagent grade salts. As such, hydration defects can therefore be expected to be present in the unprocessed material, rather than chemical impurity. Figure 12 plots IR spectra for the range 2.5–4.5 μm for samples annealed at selected temperatures close to those points in Fig. 10 where distinct changes in the relative proportions of the tetrahedral species occur (i.e. the decrease in SiO_3 and the rise in SiO_4). The 2.5–4.5 μm region is where vibrational contributions from the stretch modes of bonded Si-H, Si-OH and the symmetric stretch modes of interstitial H_2O molecules are observed in silicates. While the absence of any strong feature at 4.43 μm discounts Si-H defects from being present in significant quantities, a broad asymmetric feature is observed up to annealing temperatures of 400 °C, which is absent from the samples annealed at the higher temperatures. Efimov et al. (2003) identified eight bands in the spectral envelope between 2.7 and 4.08 μm of silicate glasses: four at 2.947, 3.125, 3.380, & 3.436 μm attributable to stretching vibrations in interstitial H_2O and four at 2.782, 2.838, 3.636 and 3.934 μm attributable to OH stretch modes in Si-OH bonded hydroxyl. A three-component fit to the broad asymmetric band in the unprocessed sample gave three distinct bands: one at 2.848 ± 0.001, which by reference to the Efimov values is attributable to OH defects and two at

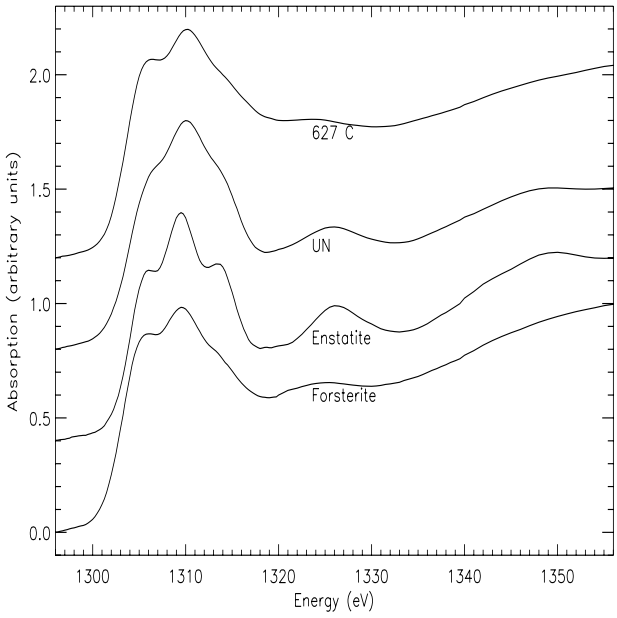

Fig. 11. Mg K-edge XANES of $MgSiO_3$ (UN and 627 °C) compared to crystalline reference samples of forsterite and Enstatite, showing the similarity between Mg site structure in the unprocessed sample and enstatite and between the annealed sample and forsterite. Data from Thompson (2008).

3.030 ± 0.005 and 3.427 ± 0.24, similarly attributable to interstitial water. Terrestrial silicate minerals exhibit H_2O loss below ~300 °C and single or multi-step dehydroxylation in the range 500–700 °C, with the dehydroxylation temperature determined primarily by the specific crystal structures and their octahedral and extra-framework cation compositions, with various intermediary crystal phases forming as dehydroxylation progresses (e.g. Che et al. 2011, and references therein). However, the dehydroxylation temperature is lowered if the mineral structure becomes disordered (Tyburczy & Ahrens 1988) suggesting that the changes we observe in the medium-range structure are related (at least above ~400 °C) to the loss of both interstitial H_2O and bonded OH.

Due to their formation in H-rich environments, bonded hydrogen defects such as SiH and SiOH have long been assumed to be present in cosmic silicates (e.g. Moore et al. 1991; Whittet et al. 1997; Timmermann & Larson 1993; Malfait et al. 1999; Thompson et al. 2003), though the proximity of O-H features from water ice in this part of the spectrum have hindered observational identifications. Hydroxylated amorphous silicates on the other hand have been indentified in interplanetary dust particles (IDPs) and glasses with embedded metal and sulphides (GEMS; Thomas et al. 1993; Bradley 1994; Bradley et al. 2005) some of which may be pre-solar (Messenger et al. 2003) and originate from the ISM (Bradley et al. 1999). The presence of OH groups in these recovered amorphous silicates is thought to result from hydrogen implantation by irradiation processes (Bradley 1994); while Djouadi et al. (2011) suggest stable OH defects in interstellar silicates should result from low energy proton irradiation in shock waves. Although levels of hydration in cosmic grains may be lower (Djouadi et al. 2011), similar changes in both medium-range structure and 10 μm band behaviour, as identified here, should also therefore be expected for cosmic silicates.

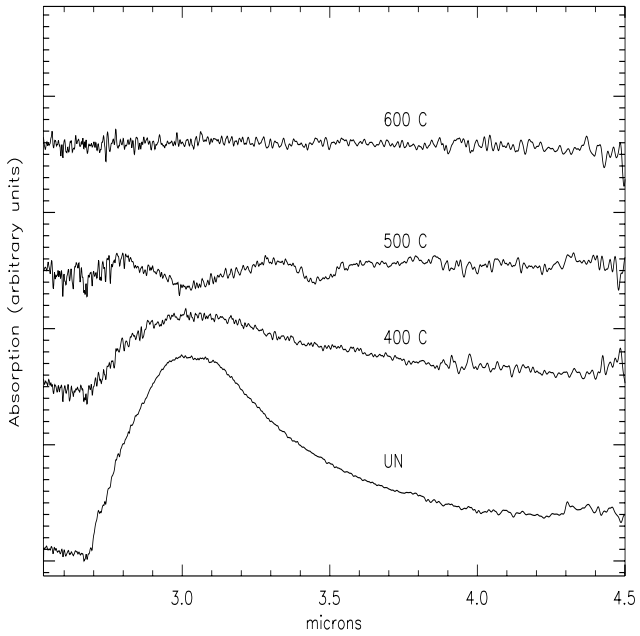

Fig. 12. 2.5 to 4.5 μm portion of the IR spectra measured for $MgSiO_3$ samples at selected annealing temperatures chosen to represent those points in Fig. 10 where the relative proportions of Si_2O_5, SiO_3 and SiO_4 exhibit strong differences. The decrease in the broad band at ~3 μm indicates a decrease in hydration through the loss of interstitial H_2O and bonded OH.

4.1.5. Other defects

Many crystalline materials exhibit the phenomenon of polymorphism where, for a given composition, crystal structures with different stable or metastable atomic arrangements can be adopted, usually selected for by external factors including, but not limited to, temperature and pressure. Examples of this are the well known SiO_2 phases quartz, tridymite and cristobalite, or the carbon phases of graphite and diamond. For non-crystalline materials the corresponding phenomenon of polyamorphism has been observed in water ice (Mishmima & Suzuki 2002), silicon (McMillan et al. 2005), and SiO_2, GeO_2, B_2O_3 & SiO_2GeO_2 oxide glasses (Grimsditch 1984; Itie et al. 1989; Polsky et al. 1999; Nicholas et al. 2004; Majérus et al. 2004). In amorphous SiO_2 the polyamorphous transition is irreversible and shifts in its Raman spectrum suggest the transition largely involves medium-range structure, with only minor changes to the short-range tetrahedral ordering (Champagnon et al. 2007). The experimental results obtained for the amorphous $MgSiO_3$ used in this study point to thermally driven transitions involving medium-range structure. If the changes we have observed are aided by the removal of hydration defects, it is also plausible that the removal of other defects (e.g. unsatisfied bonds, incomplete tetrahedral combination etc.) in cosmic grains could similarly produce amorphous to amorphous changes during grain processing. While the specific parameters describing the size and NBO/T distribution etc. of the medium-range structures in any given amorphous silicate are likely to be dependent on the conditions and processes by which it was produced, polyamorphous behaviour should be a general feature. Unlike crystalline phases, amorphous structural arrangements do not represent unique minimum energy states. The Gibbs free energy, ΔG, of an amorphous substance is always higher than that of the same substance in its crystalline state and transitions between amorphous arrangements with close, or similar, energies can occur. Grain formation in circumstellar outflows is a stochastic processes (Egan & Leung 1995) involving non-uniform periods of nucleation and growth in conditions where temperatures and densities can decrease rapidly. Highly disordered amorphous structures arise when incoming atoms or molecules either do not have sufficient energy at lower temperatures to find their optimum site in the structure, simply sticking near to where they first became bound to the grain surface or, at higher effective gas densities, may not have time to migrate before being covered by the arrival of subsequent atoms/molecules. Such a grain material with significant structural and chemical disorder, varied tetrahedral connectivitys, unsatisfied bonds and defects will occupy an energy state above the equilibrium energy of the equivalent crystalline phase suggested by its bulk composition. Subsequent thermal processing – below crystallisation temperatures – should result in the transition to lower energy, but nevertheless still amorphous (i.e. polyamorphous), structural arrangements which should, as our results demonstrate, have a measureable effect on spectroscopic behaviour since the NBO/T distribution will have changed.

5. Conclusions

The laboratory results presented in this work link the spectroscopic behaviour of the 10 μm band in amorphous $MgSiO_3$ with thermally induced changes in the silicate's medium-range structure at a level characterised by variations in the relative number and types of interconnections between tetrahedral Si-O units. The presence of medium-range structure results in weak aperiodic longer-range spatial correlations which act as pseudo-lattice planes giving rise in the laboratory to characteristic X-ray scattering features at low values of the X-ray scattering vector. In decomposing the 10 μm band into separate components, we have identified a correspondence between changes in the relative proportions of different tetrahedral species (e.g. Si_2O_5, SiO_3, etc.) and the build up and release of strain in the silicate structure, as probed by X-ray scattering and Raman spectroscopy, due to the linking and breaking of the interconnections between tetrahedra. These processes result in the adoption of new tetrahedral arrangements characterised by different bulk bridging to non-bridging oxygen distributions. The evolution of structure at this level is likely aided at higher temperatures by the loss of defects. Although the effect of varying the composition has not been explicitly examined, the results suggest that composition and spectral response (at 10 μm) have only an indirect relationship, with the dominant influence originating more directly from the medium-range structure. This will of course be influenced in part by the composition (e.g. the ratio of network formers to network modifiers), the defect content and medium-range structure will however be determined by their formation conditions. The identification of annealing induced amorphous to amorphous structural evolution and its relationship to spectral response also raises the question of whether the currently available pool of laboratory derived optical data are sufficient to model amorphous cosmic silicates in vastly different environments, or whether the details of the constraints the amorphous structure places on optical properties due to polyamorphous variations have thus far been under characterised.

Acknowledgements. This work was supported by Diamond Light Source beamtime allocation NT1185. The authors would like to thank Mr Jonathan Potter for technical assistance on the I11 beamline and extend their thanks to the anonymous referee who provided constructive and helpful comments regarding the FTIR analysis.

References

Aguiar, H., Serra, J., González, P., & León, B. 2009, J. Non-Cryst. Solids, 355, 475
Beelen, A., Cox, P., Benford, D. J., et al. 2006, ApJ, 642, 694
Boisen, M. B., Gibbs, G. V., Downs, R. T., & D'Arco, P. 1990, Am. Mineral., 75, 748
Bouwman, J., Meeus, G., de Koter, A., et al. 2001, A&A, 375, 950
Bradley, J. P. 1994, Science, 265, 925
Bradley, J. P., Keller, L. P., Snow, T. P., et al. 1999, Science, 285, 171
Bradley, J. P., Dai, Z. R., Erni, R., et al. 2005, Science, 307, 244
Brawer, S. A., & White, W. W. 1975, J. Chem. Phys., 63, 2421
Bringa, E. M., Kucheyev, S. O., & Loeffler, M. J. 2007, ApJ, 662, 372
Brucato, J. R., Colangeli, L., Mennella, V., et al. 1999, A&A, 348, 1012
Brucato, J. R., Mennella, V., Colangeli, L., et al. 2002, Planet. Space Sci., 50, 829
Brucato, J. R., Strazzulla, G., Baratta, G., & Colangeli, L. 2003, A&A, 413, 395
Champagnon, B., Martinet, C. Coussa, C., et al. 2007, J. Non-Cryst. Solids, 353, 4208
Che, C., Glotch, T. D., Bish, D. L., et al. 2011, J. Geophys. Res., 116, E05007
Chiar, J. E. M., & Tielens, A. G. G. M. 2006, ApJ, 637, 774
Clavel, J., Schulz, B., Altieri, B., et al. 2000, A&A, 357, 839
Coupeaud, A., Demyk, K., Meny, C., et al. 2011, A&A, 535, A124
Davoisine, C., Leroux, H., & Frère, M. 2008, A&A, 482, 541
Djouadi, Z., Robert, F., Le Sergeant d'Hendecourt, L., et al. 2011, A&A, 531, A96
Demyk, K., Jones, A. P., Dartois, E., et al. 1999, A&A, 349, 267
Demyk, K., Carrez, Ph., Leroux, H., et al. 2001, A&A, 368, L38
Demyk, K., d'Hendecourt, L., Leroux, H., et al. 2004, A&A, 420, 233
Dorschner, J., Begemann, B., Henning, T., et al. 1995, A&A, 300, 503
Draine, B. T. 2003, ARA&A, 41, 241
Draine, B. T., & Lee, H. M. 1984, ApJ, 285, 89
Dullemond, C. P., Apai, D., Walch, S., et al. 2006, ApJ, 64, L67
Egan, M. P., & Leung, C. M. 1995, ApJ, 444, 251
Elliot, S. R. 1991, Nature, 354, 445
Elliot, S. R. 1992, J. Phys. Condens. Matter., 4, 7661
Elvis, M., Marengo, M., & Karovska, M. 2002, ApJ, 567, L107
Efimov, A. M., Pogareva, V. G., & Shashkin, A. V. 2003, J. Non-Cryst. Solids, 332, 93
Forrest, W. J., Gillett, F. C., & Stein, W. A. 1975, ApJ, 195, 423
Furukawa, T., Fox, K. E., & White, W. B. 1981, J. Chem. Phys., 75, 3226
Gaskell, P. H. 1986, J. Non-Cryst. Solids, 75, 329
Genzel, R., Lutz, D., Sturm, E., et al. 1998, ApJ, 498, 579
Gibbs, G. V., Hamil, M. M., Louisnathan, S. J., et al. 1972, Am. Mineral., 57, 1578
Grimsditch, M. 1984, Phys. Rev., 52, 2379
Gurman, S. J. 1990, J. Non-Cryst. Solids, 125, 151
Henning, Th., Il'in, V. B., Krivova, N. A., et al. 1999, A&AS, 136, 405
Hao, L., Spoon, H. W. W., Sloan, G. C., et al. 2005, ApJ, 625, L75
Houck, J. R., Soifer, B. T., Weedman, D., et al. 2005, ApJ, 622, L105
Imai, Y., Koike, C., Chihara, H., et al. 2009, A&A, 507, 277
Itie, J. P., Polain, A., Calas, G., et al. 1989, Phys. Rev., 63, 398
Jäger, C., Mutschke, H., Begemann, B., et al. 1994, A&A, 292, 641
Jäger, C., Molster, F. J., Dorschner, J., et al. 1998, A&A, 339, 904
Jäger, C., Fabian, D., Schrempel, F., et al. 2003, A&A, 401, 57
Kalampounias, A. G., Nasikas, N. K., & Papatheodorou, G. N. 2008, J. Chem. Phys., 131, 114513
Kuniaki, K. 1990, Eur. J. Mineral., 2, 63
Kusabiraki, K. 1987, J. Non-Cryst. Sol., 95/96, 411
Kusabiraki, K., & Shiraishi, Y. 1981, J. Non-Cryst. Solids, 44, 365
Laurent, O., Mirabel, I. F., Charmandaris, V., et al. 2000, A&A, 359, 887
Lebiediev, A. A. 1921, Trans. Opt. Inst. Petr., 2, 10
Louzguine, D. V., Yavari, A. R., Ota, K., et al. 2005, J. Non-Cryst. Solids, 351, 1639
Lucovski, G., & Galeener, F. L. 1980, J. Non-Cryst. Solids, 37, 53
Maiolino, R., Marconi, A., & Oliva, E. 2001, A&A, 365, 37
Majérus, O., Cormier, L., Itie, J. P., et al. 2004, J. Non-Cryst. Solids, 345, 34
Malfait, K., Waelkens, C., Bouwman, J., et al. 1999, A&A, 345, 181
Markwick-Kemper, F., Gallagher, S. C., Hines, D. C., & Bouwman, J. 2007, ApJ, 668, L107
McDonald, W. S., & Cruickshank, D. W. J. 1967, Acta Crystallogr., 22, 37
McMillan, P. F., Wilson, M., Daisenberger, D., et al. 2005, Nature, 4, 680
Messenger, S., Keller, L. P., Stadermann, F. J., et al. 2003, Science, 300, 105
Mishima, O., & Suzuki, Y. 2002, Nature, 419, 599
Moore, M. H., Tanabe, T., & Nuth, J. A. 1991, ApJ, 373, L31
Mozzi, R. L., & Warren, A. C. 1969, J. Appl. Cryst., 2, 164
Morgan, H. L., & Edmunds, M. G. 2003, MNRAS, 343, 427
Mysen, B. O., Finger, L. W., Virgo, D., & Seifert, F. A. 1982, Am. Mineral., 67, 686
Natta, A., Testi, L., Calvet, N., et al. 2007, in Protostars and Planets V, eds. B. Reipurth, D. Jewitt, & K. Keil (University Arizona Press), 767
Nicholas, J., Sinogeikin, S., Kieffer, J., et al. 2004, Phys. Rev. Lett., 92, 215701
Nuth, J. A., & Hecht, J. H. 1990, Ap&SS, 163, 79
Nuth, J. A., & Johnson, N. M. 2006, Icarus, 180, 243
Ossi, P. M. 2003, Disordered Materials (Berlin: Springer Advanced Texts in Physics)
Pant, A. K. 1968, Acta Crist. B, 24, 1077
Pant, A. K., & Cruickshank, D. W. J. 1968, Acta Crist. B, 24, 13
Peacor, D. R. 1973, Z. Kristallogr., 138, 274
Philips, J. C. 1979, J. Non-Cryst. Solids, 34, 153
Polsky, C. H., Smith, K. H., & Wolf, G. H. 1999, J. Non-Cryst. Solids, 248, 159
Priddey, R. S., Isaak, K. G., McMahon, R. G., et al. 2003, MNRAS, 344, L74
Randall, J. T., Rooksby, H. P., & Cooper, B. S. 1930a, J. Soc. Glass Technol., 14, 219
Randall, J. T., Rooksby, H. P., & Cooper, B. S. 1930b, Z. Krist., 75, 196
Riaz, B. 2009, ApJ, 701, 571
Roche, P. F., & Aitken, D. K. 1984, MNRAS, 208, 481
Roskosz, M., Gillot, J., Capet, F., et al. 2009, ApJ, 707, L174
Rigopoulou, D., Spoon, H. W. W., Genzel, R., et al. 1999, AJ, 118, 2625
Sargent, B., Forrest, W. J., D'Alessio, P., et al. 2006, ApJ, 645, 395
Serghiou, G., Boehler, R., & Chopelas, A. 2000a, J. Phys. Condens. Matter, 12, 849
Serghiou, G., Chopelas, A., & Boehler, R. 2000b, J. Phys. Condens. Matter, 12, 8939
Serghiou, G., Chopelas, A., & Boehler, R. 2004, J. Phys. Condens. Matter, 16, S1255
Shupping, R. Y., Kassis, M., Morris, M., et al. 2006, ApJ, 644, L71
Smith, H. A., Li, A., Li, M. P., et al. 2010, ApJ, 716, 490
Stancik, A. L., & Brauns, E. B. 2008, Vibr. Spectr., 47, 66
Strum, E., Schweitzer, M., Lutz, D., et al. 2005, ApJ, 629, L21
Sugerman, B. E. K., Ercolano, B., Barlow, M. J., et al. 2006, Science, 313, 196
Tartoni, N., Thompson, S. P., Tang, C. C., et al. 2008, J. Synchrotron Rad., 15, 43
Thomas, K. L., Blanford, G. E., Keller, L. P., et al. 1993, Geochim. Cosmochim. Acta, 57, 1551
Thompson, S. P. 1996, Astrophys. Lett. Comm., 33, 299
Thompson, S. P. 2008, A&A, 484, 251
Thompson, S. P., & Tang, C. C. 2001, A&A, 368, 721
Thompson, S. P., Fonti, S., Verrienti, C., et al. 2002, A&A, 395, 705
Thompson, S. P., Fonti, S., Verrienti, C., et al. 2003, Met. Planet. Sci., 38, 457
Thompson, S. P., Verrienti, C., Fonti, S., et al. 2007, Adv. Space Res., 39, 375
Thompson, S. P., Parker, J. E., Potter, J., et al. 2009, Rev. Sci. Instr., 80, 075107
Tielens, A. G. G. M. 2003, Science, 300, 68
Timmermann, R., & Larson, H. P. 1993, ApJ, 415, 820
Tran, Q. D., Lutz, D., Genzel, R., et al. 2001, ApJ, 552, 527
Tyburczy, J. A., & Ahrens, T. J. 1988, Proc. Lunar Planet. Sci., 18th Conf., 435
Valenkow, N., & Porai-Koshitz, E. 1936, Z. Krist., 95, 195
van Boekel, R., Min, M., Waters, L. B. F. M., et al. 2005, A&A, 437, 189
Veilleux, S. 2004, in Multiwavelength AGN Surveys, eds. R. Mújica, & R. Maiolino (Singapore: World Scientific), 205
Verweij, H., & Konijnendijk, W. L. 1976, J. Am. Ceram. Soc., 59, 517
Virgo, D., Mysen, B. O., & Kushiro, I. 1980, Science, 208, 1371
Voshchinnikov, N. V., & Henning, T. 2008, A&A, 483, L9
Wang, A., Jolliff, B. L., Haskin, L. A., et al. 2001, Am. Mineral., 86, 790
Warren, B. E. 1933, Z. Krist., 86, 349
Warren, B. E. 1934, J. Am. Ceram. Soc., 17, 249
Warren, B. E., Krutter, H., & Morningstar, O. 1936, J. Am. Ceram. Soc., 19, 202
Watson, D. M., Leisenring, J. M., Furlan, E., et al. 2009, ApJS, 180, 84
Weingartner, J. C., & Draine, B. T. 2001, ApJ, 548, 296
Whittet, D. C. B., Boogert, A. C. A., Gerakines, P. A., et al. 1997, ApJ, 490, 729
Wright, A. C. 1990, J. Non-Cryst. Solids, 123, 129
Wright, A., Sinclair, R. N., & Leadbetter, A. J. 1985, J. Non-Cryst. Solids, 71, 295
Wright, A. C., Hulme, R. A., Grimley, D. I., et al. 1991, J. Non-Cryst. Solids, 129, 213
Yuan, X., & Cormack, A. N. 2003, J. Non-Cryst. Solids, 319, 31
Zachariasen, W. H. 1932, J. Am. Ceram. Soc., 17, 3841